NUCL SCI TECH (2017) 28:148
DOI 10.1007/s41365-017-0300-1

# Discovery of a novel small inhibitor RJ19 targeting to human Hsp90

**Hui-Ling Cao[1] · Kai-Kai Lyu[2] · Bin Liu[3] · Jian Li[4,5,6] · Jian-Hua He[4]**

Received: 30 May 2017 / Revised: 18 June 2017 / Accepted: 22 June 2017 / Published online: 8 September 2017


**Abstract** Heat shock protein 90 (Hsp90) can promote growth and proliferation of cancer cells by helping in folding, conformational maturation, and activation of various client proteins. Therefore, Hsp90 has been paid more attention to as an anticancer drug target. Reported Hsp90 inhibitors have several limitations such as poor solubility, limited bioavailability, and hepatotoxicity. Here, a novel small inhibitor RJ19 has been designed using fragment-based drug discovery and synthesized. Additionally, a crystal structure of $Hsp90^N$–RJ19 was determined by X-ray diffraction (resolution limit, 2.0 Å, PDB code 4L90). The crystal structure of $Hsp90^N$–RJ19 was analyzed in detail and compared with that of native $Hsp90^N$, $Hsp90^N$-ATP, and $Hsp90^N$-GDM, respectively. It was indicated that RJ19 interacted with $Hsp90^N$ at the ATP-binding pocket, which suggests that RJ19 may replace nucleotides to bind with $Hsp90^N$ to result in chaperone function failure of Hsp90. RJ19, therefore, has emerged as a promising anticancer lead compound. Rearrangement and displacement of L2 Loop in $Hsp90^N$–RJ19 play a key role in the function failure, which also makes the pocket wider and longer facilitating structure modification of RJ19 later. The complex crystal structure and interaction between RJ19 and $Hsp90^N$ provide a rational basis for the design and optimization of novel anticancer drugs.

**Keywords** Heat shock protein 90 · Drug target · Inhibitor · X-ray diffraction · Complex crystal structure

## 1 Introduction

As the most dominant technique, X-ray diffraction (XRD) determined 89.56% structures (116,200) of protein data bank (PDB, total structures 129,745, data on May 2nd,

Hui-Ling Cao and Kai-Kai Lyu have contributed equally to this work.

This work was supported by the National Natural Science Foundation of China (Nos. 31401185 and 81402850) and the Introduced talents Foundation of Xi'an Medical University (No. 2015 RCYJ 01).

**Electronic supplementary material** The online version of this article (doi:10.1007/s41365-017-0300-1) contains supplementary material, which is available to authorized users.

✉ Jian Li
Jian.li@uky.edu

✉ Jian-Hua He
hejianhua@sinap.ac.cn

[1] Shaanxi Key Laboratory of Ischemic Cardiovascular Disease, Institute of Basic and Translational Medicine, Xi'an Medical University, Xi'an 710021, China

[2] University of Chinese Academy of Sciences, Beijing 100049, China

[3] Key Laboratory of Protein Modification and Tumor, Hubei Polytechnic University School of Medicine, Huangshi 435003, China

[4] Shanghai Institute of Applied Physics, Chinese Academy of Sciences, Shanghai 201204, China

[5] Biotech and Biomedicine Science Co. Ltd., Shenyang 110000, China

[6] Department of Molecular and Cellular Biochemistry, College of Medicine, University of Kentucky, Lexington, KY 40508, USA

2017, http://www.Rcsb.org/pdb). Nowadays, XRD is a routine way to determine how a small molecular inhibitor interacts with its target and how to improve it based on ligand-target complex crystal structure, which provides detailed interactions in an active state for drug design and structure modification. As a result, XRD has become a predominant standard technique for drug discovery area [1–3].

The heat shock protein 90 (Hsp90, 90 kD) is an α–α or β–β homodimer in the cytosolic, and each monomer consists of three domains. The C-terminal domain plays a key role for dimerization of Hsp90, while the central domain possesses a large hydrophobic surface to bind client proteins and facilitate them folding. The N-terminal domain with highly conserved residues across species contains an extraordinary ATP-binding pocket that is responsible for ATP-binding and hydrolysis, which is indispensable for the chaperone function of Hsp90 [4–6]. The first crystal structure of human $Hsp90^N$ from Stebbins et al. revealed the α/β sandwich pocket in detail [7]. The pocket is about 15 Å deep, 12 Å in diameter for entrance, and 8 Å for flat-bottomed cone. The base comprises of eight antiparallel β sheets (three central β sheets, S3, S4, and S7), while the wall consists of three helices and a loop (H2-H4-H7-L1). From the entrance toward the bottom, the pocket becomes increasingly hydrophobic [4–8].

As a chaperone, Hsp90 has dual chaperone functions participating not only in the cellular stress response but also in folding or refolding, conformational maturation, and activation of a wide range of client proteins [7–11]. More than 300 Hsp90-dependent client proteins have been identified including varying eukaryotic protein kinases and nuclear hormone receptors related to multiple signaling pathways [12]. Of these, 48 client proteins are directly related to oncogenesis [10]. Hsp90 is overexpressed to facilitate these client proteins to fold and maintain their activity in malignant cells. Inhibitors of Hsp90 can interfere in Hsp90-mediated chaperone function to make the client proteins being an immature or misfolding state, which will be captured and degraded by proteasomes. With degraded proteins accumulated, multiple signaling pathways can be derailed simultaneously, which can hinder proliferation and progression of cancer [9–12]. Hsp90, therefore, has been paid more attention to as an anticancer drug target.

Hsp90 inhibitors contain C-terminal inhibitors such as novobiocin, and mainly N-terminal inhibitors such as geldanamycin (GDM) and radicicol (RDC) [12–14]. As a naturally occurring antitumor antibiotic, anticancer mechanism of GDM was unclear until GDM-$Hsp90^N$ crystal structure was determined [7]. It was suggested that GDM bound in the pocket to hinder ATP binding to $Hsp90^N$, resulting in Hsp90-mediated folding or refolding, conformational mature or activation of client proteins failed. The growth and progression of cancer, therefore, can be inhibited [7, 12–15]. Another naturally occurring antitumor antibiotic radicicol acts in the similar way [12–15]. Several derivatives of GDM have entered clinical studies, for instance, 17-AAG [16], 17-DMAG [17], and IPI-504 [18]. They, nevertheless, have several potential limitations, such as poor solubility, limited bioavailability, and hepatotoxicity [16–18]. This leads to significant efforts to discover novel inhibitors of Hsp90.

It is a major challenge in the drug discovery to find novel compounds as starting points for optimization. Fragment-based drug discovery (FBDD) has become a powerful technique to find novel compounds, which was put forward by William P Jencks in 1981 for the first time [19]. It develops based on advantages combining random screening and structure-based drug discovery (SBDD). Active fragments are discovered by random screening of built fragment library. Followed, promising compounds can be obtained by growth, jointing, and self-assembly of active fragments. Finally, novel-lead compounds will be got by several rounds of crystal structure-directed optimization. Compared with traditional method, FBDD has outstanding merits as follows: (1) to explore more chemical spaces with less fragments; (2) to find promising compounds with higher chances; (3) to find promising compounds with fine affinity and druggability with higher chances; and (4) to avoid false positive results [6, 19, 20].

Here, a novel small inhibitor RJ19 has been designed using FBDD and synthesized. In addition, the complex crystals of RJ19 and $Hsp90^N$ were grown and a high-resolution crystal structure was determined by XRD, which was deposited in PDB with accession code 4L90. The crystal structure of $Hsp90^N$–RJ19 was analyzed in detail and compared with the crystal structure of $Hsp90^N$, ATP-$Hsp90^N$, and GDM-$Hsp90^N$, respectively. The complex crystal structure and the interaction between RJ19 and $Hsp90^N$ provide a rational basis for the design and optimization of novel anticancer drugs targeting $Hsp90^N$ with superior quality.

## 2 Experimental section

### 2.1 Synthesis of small molecule

As show in Fig. 1, Compound one reacted with methanol via Oxalyl chloride to afford compound two, then followed by formylation with α,α-dichloromethyl methyl ether to obtain compound three. Construction of compound five utilized intramolecular ring-closing from compound four that was obtained by reacting with 5-Bromo-2-hydrazinopyridine and compound three. Compound five was

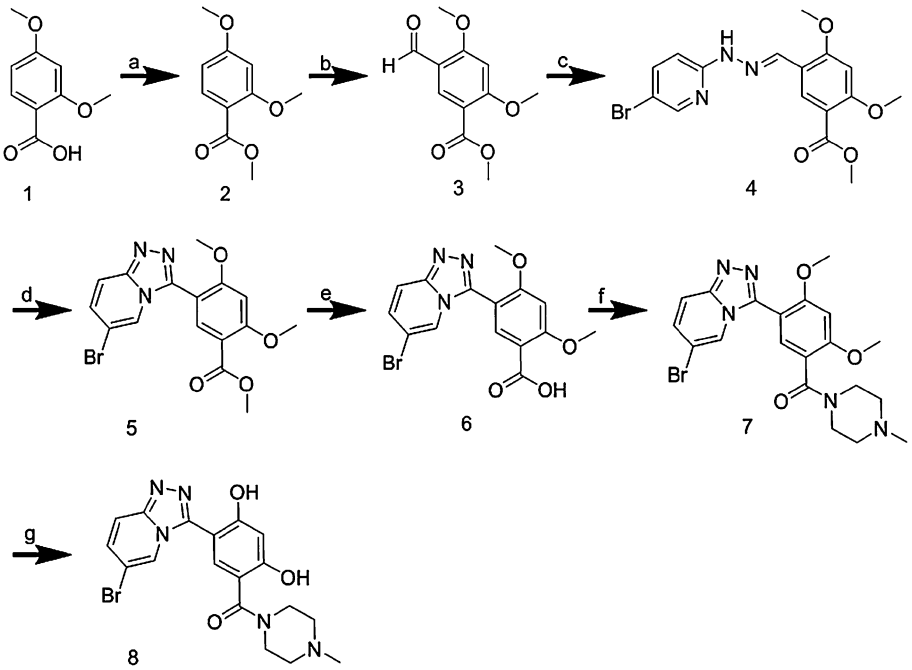


**Fig. 1** Synthesis of the small molecule RJ19. (*a*) (i) $(COCl)_2$, DMF, DCM, 0 °C-rt; (ii) MeOH, rt, 95%; (*b*) α,α-dichloromethyl methyl ether,TiCl4, DCM, 0 °C-r, 98%;(*c*) 5-Bromo-2-hydrazinopyridine, EtOH, reflux, 93%; (*d*) PhI $(OAc)_2$, DCM, MeOH, rt, 77%; (*e*) LiOH, MeOH, $H_2O$, reflux, 95%; (*f*) 1-methylpiperazine, EDCI, HOBt, DIPEA, DCM, rt, 80–85%; and (*g*) BBr3, DCM, −78 °C-rt, 13–25%

hydrolyzed with Lithium hydroxide in aqueous solutions of methanol to get compound six. Compound six was condensated with 1-methylpiperazine and deprotected by boron tribromide to obtain the target compound eight(RJ19).

## 2.2 Protein purification and crystallization

The gene of human Hsp90α N-terminal domain including residues 9–236 was cloned into a pET28a vector, which was transformed into *E. coli* Rosetta (DE3) pLysS for over-expression of drug target $Hsp90^N$ (Invitrogen, Carlsbad, America). The engineering bacteria were grown in 1000 mL luria–bertani broth (LB) at 310 K to $OD_{600}$ value of 0.6–0.8 and followed induced by 200 μM isopropyl *β*-D-thiogalacto pyranoside (IPTG) for 3–5 h at 303 K. The express bacteria were collected by centrifugation at 10,000*g* for 10 min (CF16RX, Hitachi, Japan). The precipitate was re-suspended in buffer A (pH 7.5, 0.1 M Tris–HCl, 0.3 M NaCl and 5% glycerol) and followed crushed by ultra-high-pressure cell disrupter (JN-02C, JNBIO, China). For preliminary purification, the product was centrifuged at 30,000*g* for 30 min at 277 K, and the supernatant was loaded onto a 5 mL $Ni^{2+}$-nitrilotriacetate column (Ni–NTA, GE Healthcare, America). The target protein was eluted with buffer B (pH 7.5, 0.1 M Tris–HCl, 0.3 M NaCl, 0.1 M imidazole, and 5% glycerol). The primary purified protein was concentrated, and the buffer was exchanged to buffer C(pH 7.5, 0.1 M Tris–HCl, 0.15 M NaCl, and 5% glycerol) using a 10,000 Mr cutoff centrifugal concentrator (Amicon Ultra-15, Millipore, America). For fine purification, the impurities were removed by a gel filtration column (Superdex 75 PG, GE Healthcare, America) with buffer C. The purified protein was analyzed by a 15% SDS-PAGE to determine the purity. The fine purified protein was concentrated to a concentration of about 20 mg/mL with the 10 000 Mrcut-off centrifugal concentrator again, and its concentration was determined using bicinchoninic acid method (BCA). The fine purified $Hsp90^N$ was flash-frozen with liquid nitrogen and stored at 193 K.

For crystallization, the initial concentration of target protein $Hsp90^N$ was approximately 20 mg/mL. The small molecular inhibitor RJ19 was added to protein with 5:1 molar ratio, and the mixture was incubated for 30 min at 277 K. And then the mixture was centrifuged for 10 min at 3000*g,* and the supernate was for crystallization. Co-crystallization was conducted at 277 K for 3–7 days using the hanging-drop vapor diffusion method in an incubator controlled by a bath circulator (PolyScience 9712, PolyScience, USA). The co-crystals were grown under the condition: pH 6.5, 0.2 M magnesium chloride, 0.1 M sodium cacodylate, and 20–25% (w/v) polyethylene glycol 2000 monomethyl ether (PEG2000 MME) [7].

## 2.3 Data collection, structure determination, and refinement

Co-crystals were mounted with cryo-loop (Hampton research, America) and flash-frozen in liquid nitrogen for XRD data collection. All data sets were collected at 100 K on macromolecular crystallography beamline17U1

**Table 1** Statistics for data processing and model refinement of human Hsp90$^N$–RJ19 complexes

| PDB code | 4L90 |
|---|---|
| Synchrotron | SSRF |
| Beam line | BL17U1 |
| Wavelength (Å) | 0.97920 |
| Space group | I222 |
| *a*, *b*, *c* (Å) | 69.88, 88.59, 97.98 |
| α, β, γ (°) | 90.00, 90.00, 90.00 |
| Resolution (Å) | 2.00 (2.03–2.00) |
| *R*-merge (%) | 9.2 (63.2) |
| Mean $I/\sigma$ (I) | 25.2/3.1 |
| Completeness (%) | 99.8 (100.0) |
| Redundancy | 4.9 (4.9) |
| Resolution (Å) | 36.54–2.00 |
| $R_{work}/R_{free}$ (%) | 18.80/21.94 |
| Atoms | 1751 |
| Ligand | RJ19 |
| Mean temperature factor (Å$^2$) | 27.7 |
| Bond lengths (Å) | 0.007 |
| Bond angles (°) | 1.097 |

Values in parentheses are for the highest-resolution shell

(BL17U1) at Shanghai Synchrotron Radiation Facility (SSRF, Shanghai, China) using an ADSC Quantum 315r CCD detector [21]. All the data were integrated and merged using the HKL 2000 software package [22]. The structures were determined by molecular replacement with PHENIX software [23], using the structure of Hsp90$^N$ (PDB code 3T0H) as the research model [5]. The program Coot was used to rebuild the initial model [24]. The models were refined to resolution limit 2.0 Å using the PHENIX software. The superimposed contrast was analyzed with PyMOL software package [25]. The complete data collection and refinement statistics are shown in Table 1. The coordinates and structure factors have been deposited in PDB (PDB code 4L90).

## 3 Results and discussion

### 3.1 Purification, crystallization, and structure determination of Hsp90$^N$–RJ19

Hsp90$^N$ was purified to apparent homogeneity using metal chelating chromatography, followed by gel filtration chromatography. The single elution volume peak accords with monomeric Hsp90$^N$ with a molecular weight of 25 kDa and showed a good purity which was assessed by SDS-PAGE to be 98% (as shown in Fig. S1).

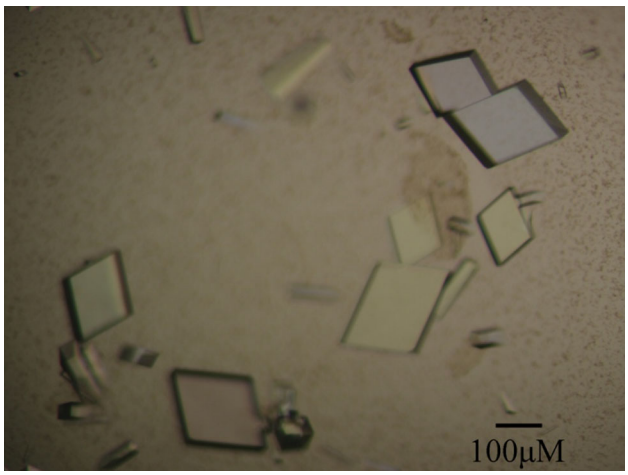


**Fig. 2** (Color online) The complex crystals of the Hsp90$^N$–RJ19 obtained by the hanging-drop method at 277 K. The average dimension of the crystals was approximately 200 μm × 100 μm × 50 μm

After 3–5 days, complex crystals of Hsp90$^N$–RJ19 were obtained by the hanging-drop method at 277 K. The average dimension of the crystals was approximately 200 μm × 100 μm × 50 μm, as shown in Fig. 2.

The structure of Hsp90$^N$–RJ19 was determined by molecular replacement using Hsp90$^N$ (PDB code 3T0H) as their search model [5]. The complete data collection and refinement statistics are shown in Table 1. The coordinates have been deposited in PDB (PDB code 4L90). Diffraction data were collected to 2.0 Å resolution and indexed in space groups $P2_12_12_1$. The unit cell parameters were as follows: $a = 69.88$ Å, $b = 88.59$ Å, and $c = 97.98$ Å; $\alpha = \beta = \gamma = 90.00°$. The refined model contains residues Val17-Lys224, and no electron density was observed for residues Asp9-Glu16 and Glu225-Glu236 in the structure. It is conceivable that the missing residues at the N- and C-termini of the model could be disordered electron density.

### 3.2 Analysis of crystal structure and interaction of Hsp90$^N$–RJ19

It was indicated from the complex crystal structure that RJ19 bound to the ATP-binding pocket completely and its intact electron density has been captured (as shown in Fig. S2). The N-terminal domain of human Hsp90 contains a highly conserved ATP-binding pocket about 15 Å deep with α/β sandwich structure. Eight uninterrupted antiparallel β-sheets constitute the pocket base. The pocket walls are formed by three α-helices and a loop, H2-H4-H7-L1 [7].

The H4-L2-H5-H6 secondary structure elements (residues 99–134) is called ATP lid. The ATP lid has open or

close conformation which is responsible for regulating pocket size and accessibility. Only when the pocket is in an open conformation, Hsp90 can bind with ATP and interact with its client proteins to accomplish folding or refolding, conformational maturation, and activation of client proteins [7–12].

A superimposing correlation was analyzed with PyMOL software between the crystal structure of $Hsp90^N$–RJ19 and $Hsp90^N$, ATP-$Hsp90^N$ or GDM-$Hsp90^N$. It was indicated that the refined crystal structure of $Hsp90^N$–RJ19 (PDB code 4L90) differed from that of $Hsp90^N$ (PDB code 3T0H), $Hsp90^N$-ATP (PDB code 3T0Z), or $Hsp90^N$-GDM (PDB code 1YET) in resolution level, as shown in Fig. 4. Their crystal packing patterns are of difference too, $Hsp90^N$–RJ19 ($P2_12_12_1$), $Hsp90^N$ ($I222$), $Hsp90^N$-ATP ($P21$), and $Hsp90^N$-GDM ($P12_11$).

As can be seen from Fig. 3a, there are some subtle differences from residues Ala101 to Phe138 in the crystal structures of $Hsp90^N$–RJ19 and native $Hsp90^N$. Figure 3c shows that the complex crystal structure of $Hsp90^N$–RJ19 differs from $Hsp90^N$-ATP from residues Asp102 to Phe138. It is different from residues Ile104 to Gly137 in the complex crystal structure of $Hsp90^N$–RJ19 and $Hsp90^N$-GDM, as shown in Fig. 3e.

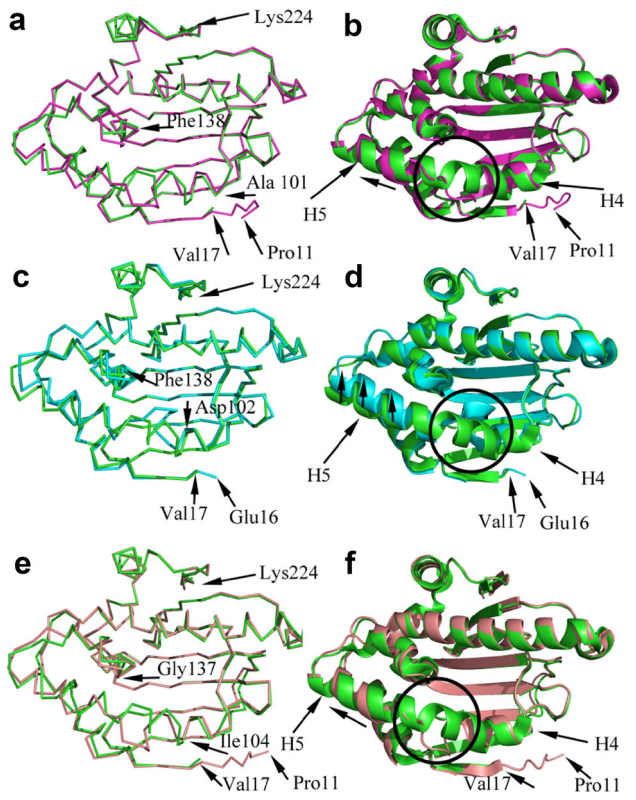


**Fig. 3** (Color online) Comparison of crystal structures of $Hsp90^N$–RJ19 with Hsp90, $Hsp90^N$-ATP and $Hsp90^N$-GDM. Superimposition of crystal structure of $Hsp90^N$–RJ19 (*green*) with $Hsp90^N$ (*magenta*): ribbon (**a**) and cartoon (**b**). Superimposition of crystal structure of $Hsp90^N$–RJ19 (*green*) and $Hsp90^N$-ATP (*cyan*): ribbon (**c**) and cartoon (**d**). Superimposition of crystal structure of $Hsp90^N$–RJ19 (*green*) and $Hsp90^N$-GDM (*pink*): ribbon (**e**) and cartoon (**f**)

The superimposition of crystal structure of $Hsp90^N$–RJ19 with native $Hsp90^N$ (Fig. 3b) shows that the H4 helix (residues from Thr99 to Leu107) and H5 helix (residues from Thr114 to Ala124) of $Hsp90^N$ undergo a conformational rearrangement after binding RJ19, which impels the L2 loop (residues from Leu107 to Thr114) in $Hsp90^N$–RJ19 rearranging and displacing to substitute portion of H4 helix as the pocket wall. L2 loop, therefore, acts as a switch to constrain the pocket entrance in diameter from 12 to 8 Å. Then, the pocket turns to a close conformation, resulting in disabled ATP binding and failed chaperone function. The rearrangement and displacement of L2 play an important role in function failure of Hsp90. The result is in accordance with that of Stebbins's [7].

The superimposition of $Hsp90^N$–RJ19 and $Hsp90^N$-ATP (Fig. 3d), $Hsp90^N$-GDM (Fig. 3f) indicates that there are differences in H4 helix, H5 helix, or L2 loop, although RJ19, ATP, and GDM all bind in the pocket, which imply their binding ways are different.

Figure 4 shows the electrostatic potential surface distribution surrounding the active pocket of $Hsp90^N$ (Fig. 4a), $Hsp90^N$-ATP (Fig. 4b), $Hsp90^N$–RJ19(Fig. 4c), and $Hsp90^N$-GDM (Fig. 4d). Compared with native $Hsp90^N$, changes have been taken place in the electrostatic potential surface surrounding the active pocket of $Hsp90^N$ responsible for binding of ATP, RJ19, or GDM. In common with the structure of ATP-$Hsp90^N$, RJ19or GDM binding site of Hsp90 is located in the ATP-binding pocket. It is interesting that RJ19 binding induces structural rearrangements of L2 loop and makes the ATP-binding pocket wider and longer, which provides a larger room for structural modification of RJ19 later.

Figure 5 shows the crystal structural superimposition of $Hsp90^N$–RJ19 (PDB code 4L90) with $Hsp90^N$-GDM (PDB code 1YET), $Hsp90^N$-17-DMAG (PDB code 1OSF), $Hsp90^N$-Onalespib (PDB code 2XJX), $Hsp90^N$-NMS-E973 (PDB code 4BQG), and $Hsp90^N$-NVP (PDB code 5JZN). It is revealed that the RJ19, GDM, 17-DMAG, Onalespib, NMS-E973, and NVP occupied the same location and there are some tiny differences in the chemical group. It is notable that in the complex of $Hsp90^N$-GDM, GDM nearly occupies the whole binding pocket, and there is no much room for structure modification. It is, therefore, significant changes were rare in solubility, bioavailability, and hepatotoxicity in derivatives of GDM. The situation, however, is different for RJ19, and there is enough room for redesigning and modification of RJ19 to obtain derivatives with high efficiency and low toxicity.

The pocket is mostly polar at its entrance, so hydrophilic groups, which can interact with polar amino acids, can be

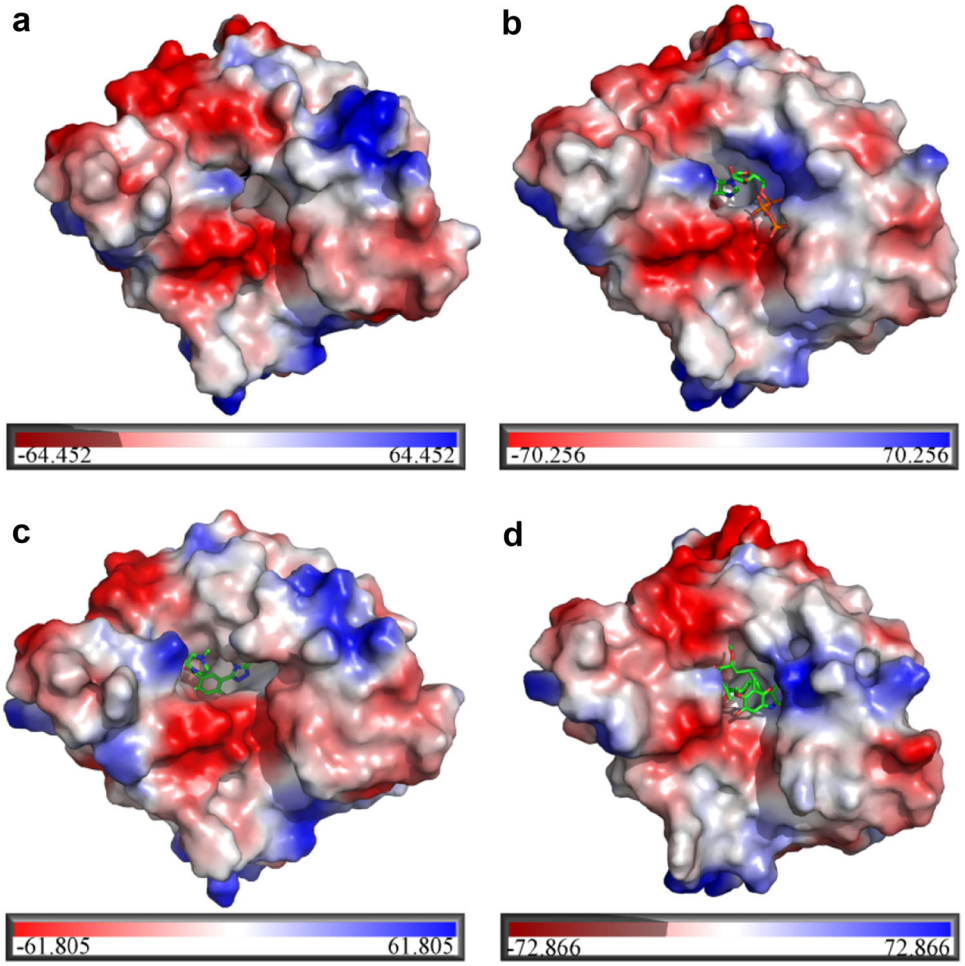


**Fig. 4** (Color online) Electrostatic potential surface distribution of crystal structure of $Hsp90^N$ and its complexes. **a** Hsp90, **b** $Hsp90^N$-ATP, **c** $Hsp90^N$–RJ19, and **d** $Hsp90^N$-GDM. The crystal structure surface is *colored* to reflect the electrostatic potential, *red* for negative charge and *blue* for positive charge, RH19, ATP, and GDM in stick representation

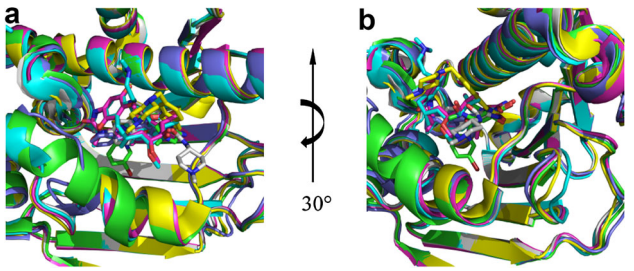


**Fig. 5** (Color online) Crystal structural superimposition of $Hsp90^N$–RJ19 (*green*) with $Hsp90^N$-GDM (*purple*), $Hsp90^N$-17-DMAG (*cyan*), $Hsp90^N$-Onalespib (*yellow*), $Hsp90^N$-NMS-E973 (*grey*), and $Hsp90^N$-NVP (*blue*). **a** Crystal structural superimposition. **b** Rotating 30° in anticlockwise. The small molecules including RJ19, GDM, 17-DMAG, Onalespib, NMS-E973, NVP, and target $Hsp90^N$ present in stick and cartoon, respectively

added to RJ19 to increase the solubility of small molecule. While it becomes predominantly hydrophobic near the pocket base, derivatives with increased affinity with Hsp90 may be yielded if groups with non-hydrogen atoms are added to RJ19 and hydrogen bond complementarity is increased.

The ATP lid consists of the H4-L2-H5-H6 secondary structure elements. It has open or close two different conformations which are responsible for regulating pocket size and accessibility [7]. The pocket in open conformation is about 12 Å in diameter near its entrance. When small molecular inhibitor RJ19 binds to the pocket, H4 and H5 helixes undergo helix-to-coil and coil-to-helix transitions, which impels L2 loop rearranging, rolling-over 180°, and moving toward the pocket to replace portion of H4 helix as one of the pocket walls. The L2 loop, therefore, acts as a switch to constrict the pocket entrance from a width of 12–8 Å. Then, the pocket changes into closed conformation, which results in disabled ATP binding and chaperone function failure. The rearrangement and displacement of L2 loop play a key role in chaperone function failure. Various client proteins being immature or misfolding state, therefore, can be captured and degraded by proteasomes. And then, the cancer cells can be inhibited. RJ19, as a result, become a hopeful lead compound.

As can be seen from Fig. 6b, there are two hydroxyls in the benzene of RJ19. The 4-hydroxyl near the isopropyl forms water-mediated hydrogen bonds with residue Ser52.

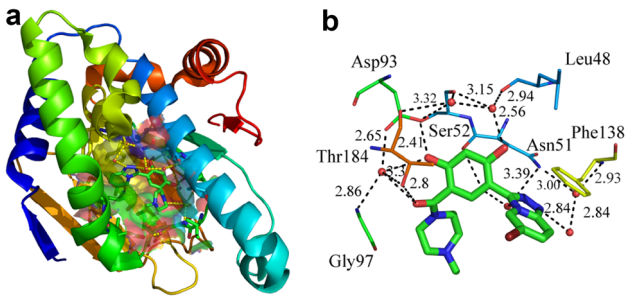


**Fig. 6** (Color online) Interaction between Hsp90$^N$ and RJ19. **a** Surface representation of RJ19 bound in the pocket of Hsp90$^N$, RJ19 ,and Hsp90 present in stick and cartoon, respectively. **b** Interactions between RJ19 and Hsp90$^N$. Carbon, nitrogen, and oxygen atoms in RJ19 are shown in *green*, *blue,* and *red*, respectively. Hydrogen bonds are shown by *black dashed lines* with distance between two atoms labeled. *Red* spheres represent water molecules

The 2-hydroxyl forms a direct hydrogen bond with residue Asp93 (distance, 2.4 Å) and three water-mediated hydrogen bonds with residue Asp93, Gly97, and Thr184, respectively. The carbonyl of RJ19 forms a direct hydrogen bond with residue Thr184 (distance, 2.8 Å) and three water-mediated hydrogen bonds with residue Asp93, Gly97, and Thr184, respectively. The hydrogen bonds or water-mediated hydrogen bonds play a dominant role in keeping fine affinity between RJ19 and Hsp90$^N$. In addition, extensive surface complementarity between RJ19 and the pocket results in a high density of van der Waals contacts, which also contribute to firmly binding of RJ19 and Hsp90$^N$.

The complex structure of Hsp90$^N$–RJ19 and interaction provide the structural basis to further investigate the activated conformational change of Hsp90 after RJ19 binding, also for redesign and structure modification of RJ19.

## 4 Conclusion

1. A novel anticancer small inhibitor RJ19 has been designed using FBDD and synthesized.
2. Hsp90$^N$–RJ19 crystal structure was determined by XRD (2.0 Å), which was deposited in PDB with accession codes 4L90.
3. RJ19 interacts with Hsp90$^N$ at the ATP-binding pocket, which suggests that RJ19 may replace nucleotides to bind with Hsp90$^N$ to disable chaperone function of Hsp90 to inhibit growth and progression of cancer. RJ19, therefore, can be a potential anticancer lead compound.
4. The rearrangement and displacement of L2 loop in Hsp90$^N$–RJ19 play an important role in function failure of Hsp90, which also makes ATP-binding pocket wider and longer and provides a larger room for redesign and structural modification of RJ19 later.
5. The complex crystal structure and the interaction between RJ19 and Hsp90$^N$ provide a scientific basis for the design and optimization of novel anticancer drugs targeting Hsp90$^N$.

## References


1. J. Ren, M. Yang, H.C. Liu et al., Multi-substituted 8-aminoimidazo [1,2-a]pyrazines by Groebke–Blackburn–Bienaymé reaction and their Hsp90 inhibitory activity. Org. Biomol. Chem. **13**(5), 1531–1535 (2015). doi:10.1039/c4ob01865f
2. H.L. Cao, L.H. Sun, L. Liu et al., Structural consistency analysis of recombinant and wild-type human serum albumin. J. Mol. Struct. **1127**, 1–5 (2017). doi:10.1016/j.molstruc.2016.07.057
3. J. Li, F. Shi, D.Q. Chen et al., FS23 binds to the N-terminal domain of human Hsp90: a novel small inhibitor for Hsp90. Nucl. Sci. Tech. **26**, 060503 (2015). doi:10.13538/j.1001-8042/nst.26.060503
4. C. Prodromou, B. Panaretou, S. Chohan et al., The ATPase cycle of Hsp90 drives a molecular 'clamp' via transient dimerization of the *N*-terminal domains. EMBO J. **19**, 4383–4392 (2000). doi:10.1093/emboj/19.16.4383
5. J. Li, L.H. Sun, C.Y. Xu et al., Structure insights into mechanisms of ATP hydrolysis and the activation of human heat-shock protein 90. Acta Biochim. Biophys. Sin. **44**, 300–306 (2012). doi:10.1093/abbs/gms001
6. C.W. Murray, M.L. Verdonkvnd, D.C. Ree, Experiences in fragment-based drug discovery. Trends Pharmacol. Sci. **33**, 224–232 (2010). doi:10.1016/j.tips.2012.02.006
7. C.E. Stebbins, A.A. Russo, C. Schneider et al., Crystal structure of an Hsp90–geldanamycin complex: targeting of a protein chaperone by an antitumor agent. Cell **89**, 239–250 (1997). doi:10.1016/S0092-8674(00)80203-2
8. N. Sung, J. Lee, J.H. Kim et al., Mitochondrial Hsp90 is a ligand-activated molecular chaperone coupling ATP binding to dimer closure through a coiled-coil intermediate. Proc. Natl. Acad. Sci. USA **113**, 2952–2957 (2016). doi:10.1073/pnas.1516167113
9. P. Meyer, C. Prodromou, B. Hu et al., Structural and functional analysis of the middle segment of Hsp 90: implications for ATP hydrolysis and client protein and cochaperoneinteractions. Mol. Cell **11**, 647–658 (2003). doi:10.1016/S1097-2765(03)00065-0
10. L.H. Galam, M.K. Hadden, Z.Q. Ma et al., High-throughput assay for the identification of Hsp90 inhibitors based on Hsp90-dependent refolding of firefly luciferase. Bioorg. Med. Chem. **15**, 1939–1946 (2007). doi:10.1016/j.bmc.2007.01.004
11. J. Li, S. Joann, B. Johannes et al., The Hsp90 chaperone machinery: conformational dynamics and regulation by co-chaperones. Biochim. Biophys. Acta **1823**, 624–635 (2012). doi:10.1016/j.bbamcr.2011.09.003
12. G. Garg, H. Zhao, B.S.J. Blagg et al., Design, synthesis and biological evaluation of alkylamino biphenylamides as Hsp90 C-terminal inhibitors. Bioorg. Med. Chem. **25**, 451–457 (2017). doi:10.1016/j.bmc.2016.11.030
13. D. Chen, A. Shen, J. Li et al., Discovery of potent N-(isoxazol-5-yl)amides as HSP90 inhibitors. Eur. J. Med. Chem. **87**, 765–781 (2014). doi:10.1016/j.ejmech.2014.09.065
14. C. Zhang, X. Wang, H. Liu et al., Design, synthesis and pharmacological evaluation of 4,5-diarylisoxazols bearing amino acid residues within the 3-amido motif as potent heat shock protein 90

(Hsp90) inhibitors. Eur. J. Med. Chem. **125**, 315–326 (2017). doi:10.1016/j.bbamcr.2011.09.003
15. J. Komal, S.O. Ochiana, P.D. Mark et al., Heat shock protein 90 inhibitors in the treatment of cancer: current status and future directions. Expert Opin. Investig. Drugs **23**, 611–628 (2014). doi:10.1517/13543784.2014.902442
16. S. Tukaj, K. Biebe, K. Kleszczynski et al., Topically applied Hsp90 blocker 17-AAG inhibits autoantibody-mediated blister-inducing cutaneous inflammation. J. Invest. Dermatol. **8**, 26169–26184 (2016). doi:10.1016/j.jid.2016.08.032
17. Z.Z. Huang, X.Q. Zhou, Y.F. He et al., Hyperthermia enhances 17-DMAG efficacy in hepatocellular carcinoma cells with aggravated DNA damage and impaired G2/M transition. Sci. Rep. **6**, 38072 (2016). doi:10.1038/srep38072
18. J.R. Sydor, E. Normant, C.S. Pien et al., Development of 17-allylamino-17- demethoxygeldanamycin hydroquinone hydrochloride (IPI-504), an anti-cancer agent directed against Hsp90. Proc. Natl. Acad. Sci. USA **103**, 17408–17413 (2006). doi:10.1073/pnas.0608372103
19. W.P. Jencks, On the attribution and additivity of binding energies. Proc. Natl. Acad. Sci. USA **78**, 4046–4050 (1981). doi:10.1073/pnas.78.7.4046
20. J. Ren, J. Li, Y. Wang et al., Identification of 'ew series of potent diphenol HSP90 inhibitors by fragment merging and structure-based optimization. Bioorg. Med. Chem. Lett. **24**, 2525–2529 (2014). doi:10.1016/j.bmcl.2014.03.100
21. Q.S. Wang, F. Yu, S. Huang et al., The macromolecular crystallography beamline of SSRF. Nucl. Sci. Tech. **26**, 010102 (2015). doi:10.13538/j.1001-8042/nst.26.010102
22. Z. Otwinowski, W. Minor, Processing of X-ray diffraction data collected in oscillation mode. Methods Enzymol. **276**, 307–326 (1997). doi:10.1016/S0076-6879(97)76066-X
23. P.D. Adams, P.V. Afonine, G. Bunkocz et al., PHENIX: a comprehensive Python-based system for macromolecular structure solution. Acta Crystallogr. D **66**, 213–221 (2010). doi:10.1107/S0907444909052925
24. P. Emsley, K. Cowta, Coot: model-building tools for molecular graphics. Acta Crystallogr. D **60**, 2126–2132 (2004). doi:10.1107/S0907444904019158
25. L. Grell, C. Parkin, L. Slatest et al., A tool for simplifying molecular viewing in PyMOL. Biochem. Mol. Biol. Educ. **34**, 402–407 (2006). doi:10.1002/bmb.2006.494034062672